Chinese Chemical Letters 33 (2022) 3925–3930

Contents lists available at ScienceDirect

Chinese Chemical Letters

journal homepage: www.elsevier.com/locate/cclet

3D multicore-shell CoSn nanoboxes encapsulated in porous carbon as anode for lithium-ion batteries

Daxu Zhang[a], Gen Chen[a,d,*], Haoji Wang[a], Long Chen[a], Ziwei Guo[a], Zuxin Wen[a], Ning Zhang[a,d], Xiaohe Liu[a,b,d,*], Renzhi Ma[c]

[a] School of Materials Science and Engineering, Central South University, Changsha 410083, China
[b] School of Chemical Engineering and Energy, Zhengzhou University, Zhengzhou 450001, China
[c] International Center for Materials Nanoarchitectonics (WPI-MANA), National Institute for Materials Science (NIMS), Ibaraki 305-0044, Japan
[d] Key Laboratory of Electronic Packaging and Advanced Functional Materials of Hunan Province, Central South University, Changsha 410083, China

ARTICLE INFO

Article history:
Received 16 August 2021
Revised 4 October 2021
Accepted 4 November 2021
Available online 11 November 2021

Keywords:
Lithium-ion battery
CoSn nanoalloys
Multicore-shell nanobox
Hydrothermal reaction
Sacrificial template

ABSTRACT

Due to its high theoretical capacity and appropriate potential platform, tin-based alloy materials are expected to be a competitive candidate for the next-generation high performance anodes of lithium-ion batteries. Nevertheless, the immense volume change during the lithium-ion insert process leads to severe disadvantages of structural damage and capacity fade, which limits its practical application. In this work, a three-dimensional (3D) multicore-shell hollow nanobox encapsulated by carbon layer is obtained *via* a three-step method of hydrothermal reaction, annealing and alkali etching. During the electrochemical reactions, the CoSn@void@C nanoboxes provide internal space to compensate the volumetric change upon the lithiation of Sn, while the inactive component of Co acts as chemical buffers to withstand the anisotropic expansion of nanoparticles. Owing to the above-mentioned advantages, the elaborated anode delivers an excellent capacity of 788.2 mAh/g at 100 mA/g after 100 cycles and considerable capacity retention of 519.2 mAh/g even at a high current density of 1 A/g after 300 cycles. The superior stability and high performance indicate its capability as promising anodes for lithium-ion batteries.

The extensive usage and urgent demand for clean energy sources require the effective exploitation and utilization of sustainable energy storage devices [1–4]. Nowadays, lithium-ion batteries (LIBs) have been intensively applied in portable electronics, electric vehicles (EV) and hybrid electric vehicles (HEV), owing to the relatively superior merits embodied in the high energy density, prolonged cycling life and low self-discharge [5,6]. However, the commercial graphite electrodes, with an insufficient theoretical capacity of 372 mAh/g and poor cycle stability, can hardly meet the ever-growing requirements of the high-capacity rechargeable batteries [7]. Tremendous efforts have also been made to explore alternative anode materials, and in this regard, metallic Sn and its alloys are promising candidates for LIBs due to its high theoretical capacity (993 mAh/g), low discharge potential (~0.5 V), large electrical conductivity and natural abundance [8–11]. Whereas, identified with most of the alloy-type materials, severe aggregation and huge volume change (over 259%) during the alloying/dealloying process can give rise to the drastic pulverization, deterioration of electric contact and incessant growth of solid electrolyte interphase (SEI), and thereby hinder the improvement of cycle lifespan and further wide applications [12–15]

To alleviate the above inadequacies, a series of helpful strategies have been investigated, including nanoparticles, alloying compounds, hollow or yolk-shell nanostructures and carbon composites [16–21]. The introduction of conductive carbon materials, which leads to the improvement of electronic conductivity and lithium-ion diffusibility, is not only used to modify the metallic Sn nanoparticles but also fabricate a carbon shell to sustain volume variation [22–25]. Therefore, the reversible capacity and structural stability can be enhanced prominently. Simultaneously, some Sn-based intermetallic compounds have been lucubrated as another effective strategy. It is worth noting that Sb, Zn, Al, *etc.* with Sn nanoparticles can alloy with Li and show synergistic effects contribution to the high reversible capacity [26–29]. Nevertheless, other inactive metal components such as Co, Fe, Mn, cannot store lithium but play a critical role as a buffer matrix to increase the conductivity and adapt anisotropic expansion of Sn active nanoparticles [30–34]. Besides, the fabrication of nanobox structure can

* Corresponding authors.
E-mail addresses: geenchen@csu.edu.cn (G. Chen), liuxiaohe@zzu.edu.cn (X. Liu).

https://doi.org/10.1016/j.cclet.2021.11.021
1001-8417/

provide additional inner space to accommodate the volume expansion, compared with the nanocube structure. In view of this, it is believed that the combination of Sn-based bimetallic compounds, tailored carbon shell and reserved void space may be an optimal selection to enhance the lithium storage properties to some extent [35,36].

Herein, a characteristic 3D hollow nanobox structure was fabricated *via* a facile strategy, in which monodisperse Sn and Co nanoalloys were completely encapsulated in carbon shell. $CoSn(OH)_6$ was employed as a metal hydroxide precursor to generate the CoSn alloy, coated by a SiO_2 layer served as the sacrificial agent and a carbon layer derived from glucose. Specifically, the SiO_2 interlayer was finally etched by NaOH in order to provide greater buffer cavities between the metal cores and the carbon shell in the unique structure [37,38]. Practically, such 3D multicore-shell nanobox structure exhibits intrinsic functions including the reservation of void space, the formation of stable SEI layer, and the release of mechanical strain. Owing to the various advantages mentioned above, the elaborated CoSn@void@C nanoboxes perform the especially outstanding reversible capacity and prolonged cycling stability as the anode for LIBs.

Cobalt Chloride Hexahydrate ($CoCl_2{\cdot}6H_2O$, 98%), tin chloride pentahydrate ($SnCl_4{\cdot}5H_2O$, 98%), tetraethyl orthosilicate (TEOS, 28.4%) and glucose ($C_6H_{12}O_6$) were all purchased from Sinopharm Chemical Reagent Co., Ltd. All reagents were analytical grade and used without further purification.

The $CoSn(OH)_6$ nanoboxes were synthesized by a reported method with some minor modifications [39]. Namely, 4 mmol $CoCl_2{\cdot}6H_2O$ and 4 mmol sodium citrate dihydrate ($Na_3C_6H_{15}O_7{\cdot}2H_2O$, ≥99%) was added into 140 mL deionized water. Afterwards, 20 mL of 0.2 mol/L $SnCl_4{\cdot}5H_2O$ alcoholic solution and 20 mL of 8 mol/L NaOH aqueous solution were dropwise added into the above solution with magnetic stirring for 1 h under 25 °C, respectively. After centrifugated with deionized water for several times and dried at 60 °C overnight, $CoSn(OH)_6$ nanoboxes were obtained as the pink precipitates. Concerning $CoSn(OH)_6$ nanocubes, a typical synthesis process was prepared by briefly changing the concentration of NaOH to 2 mol/L.

A solvothermal deposition was introduced to synthesize CoSn@void@C. Typically, 100 mg of $CoSn(OH)_6$ nanoboxes were dispersed in 70 mL distilled water and 10 mL ethanol, then 3 mL ammonium hydroxide and 700 μL tetraethyl orthosilicate were added into the above solution drop by drop. The $CoSn(OH)_6@SiO_2$ was harvested through ultrasonic dispersion, centrifugation and drying overnight. Next, the resultant $CoSn(OH)_6@SiO_2$ and 1 g glucose were immersed in 40 mL deionized water and then transferred into a 50 mL Teflon-lined stainless-steel autoclave and maintained at 180 °C for 6 h. Subsequently after cooling down to room temperature, as-formed samples were heated to 500 °C for 2 h at the ramping rate of 2 °C/min in a tube furnace under a gas mixture of Ar (95%)/H_2 (5%). Finally, CoSn@void@C nanoboxes (CSVC-NB) were obtained after treated in the solution of 2 mol/L NaOH for 1 h and dried overnight under vacuum. For comparison, CoSn@void@C nanocubes (CSVC-NC) were fabricated *via* the same procedures and bare CoSn nanoparticles were produced by annealing $CoSn(OH)_6$ nanocubes directly.

The crystallographic information of specimens was characterized using a Rigaku MiniFlex 600 diffractometer with non-monochromated Cu Kα X-ray source ($\lambda = 1.5405$ Å), operating at 40 kV voltage and 30 mA current. Field-emission scanning electron microscopy (FE-SEM, Sirion 200, 15 kV) was carried out to determine the surface morphologies and transmission electron microscopy (TEM, Tecnai G2 F20, 200 kV), coupled with energy-dispersive X-ray spectroscopy (EDX) was performed to inspect the inner morphologies and element distribution. The Raman spectra were investigated by a LabRAM HR800 system and the X-ray photoelectron spectroscopy (XPS) spectra were analyzed with a Thermo ESCALAB 250Xi spectrophotometer.

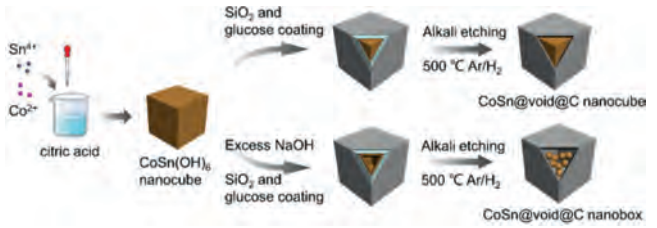

Scheme 1. Schematic illustration of the synthesis procedure of CSVC-NC and CSVC-NB.

The electrochemical performances of CoSn@void@C composites were measured with CR-2025 coin cells using a battery test system (CT2001A, Wuhan LAND Electronic, China). Half-cells were all assembled in an argon-filled glovebox (Mikrouna, China) with H_2O and O_2 content less than 0.1 ppm using Celgard 2400 polymer films as the separator, Li metal sheet as the counter and reference electrode, 1 mol/L $LiPF_6$ in a mixture of ethylene carbonate, dimethyl carbonate and ethyl methyl carbon (EC/DMC/EMC, 1:1:1 by volume) with 10 wt% fluoroethylene carbonate (FEC) as the electrolyte. The anode was fabricated as a uniform slurry by mixing the active materials, acetylene black, sodium carboxymethyl cellulose (CMC) and polyacrylic acid (PAA) with a mass ratio of 7:1:1:1. Then, the obtained slurry was coated equably on a copper-foil substrate, dried at 80 °C in vacuum overnight and then punched into round slices (diameter = 1 cm) with average loading mass of 0.8–1.0 mg/cm^2. For electrochemical measurements, cyclic voltammetry (CV) curves were conducted on electrochemical workstation (CHI-660D) in the potential 0.01–3.0 V with various scan rates. Galvanostatic charge and discharge (GCD) tests at different current densities were performed within a voltage window from 0.01 V to 3.0 V *vs.* Li^+/Li. Electrochemical impedance spectroscopy (EIS) was evaluated in a frequency domain of 100 kHz-0.01 Hz at an amplitude of 5 mV.

A typical synthesis route of CoSn@void@C composites is illustrated in Scheme 1. Firstly, $SnCl_4{\cdot}5H_2O$ and $CoCl_2{\cdot}6H_2O$ as the tin source and cobalt source were mixed together to obtain the homogeneous solution of $CoSn(OH)_6$. It is worth noting that the substantial complexation interaction among citric acid, Sn^{4+} and Co^{2+} ensures the uniform disperse of the metal source due to the abundant carboxyl in citric acid (Eq. 1) [39]. As the co-precipitation precursor, $CoSn(OH)_6$ nanocubes show a smooth cubic morphology and a mean diameter of approximately 150 nm, as shown in Fig. 1a, Figs. S1b and c (Supporting information). Next, a thin SiO_2 layer coated on the surface of $CoSn(OH)_6$ was successively synthesized using a Stöber process by adding tetraethyl orthosilicate to the $CoSn(OH)_6$ alkaline solution under ultrasonic dispersion [40]. It can be seen from the TEM images in Fig. S1d (Supporting information) that the average thickness of SiO_2 layer is about 5 nm. Subsequently, glucose was added as carbon source and conformally coated on the $CoSn(OH)_6@SiO_2$ by a hydrothermal method and then the intermediate was converted into $CoSn@SiO_2@C$ after annealing at 500 °C for 2 h under Ar (95%)/H_2 (5%) atmosphere. Finally, the obtained product was dissolved in 2 mol/L NaOH to remove the SiO_2 interlayer for making void space. While in the high alkaline medium of 8 mol/L NaOH, $CoSn(OH)_6$ could react with excess OH^- to form soluble complexes, which led to the formation of the elaborated multicore CoSn@void@C nanoboxes (CSVC-NB). Especially for comparison, bare CoSn nanoparticles were produced by annealing $CoSn(OH)_6$ precursor directly, with irregular morphology features as shown in Fig. S1a (Supporting information).

The scanning electron microscope (SEM) and transmission electron microscope (TEM) images for CSVC-NC and CSVC-NB are de-

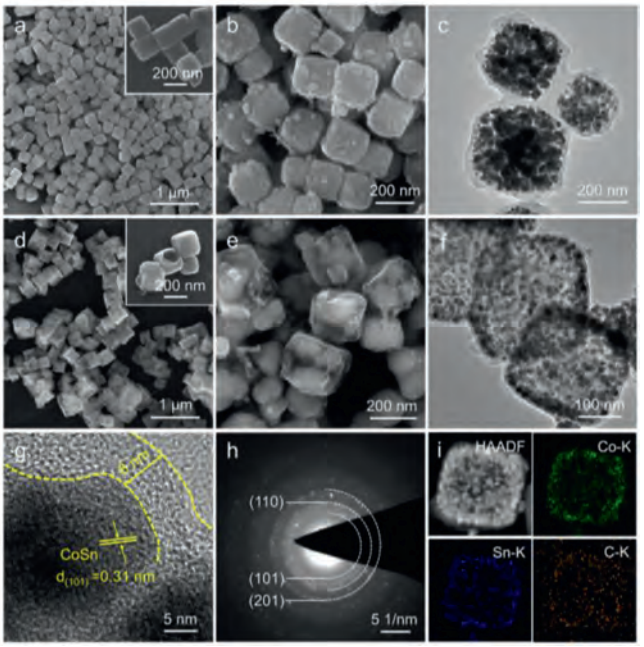

Fig. 1. (a) SEM image of $CoSn(OH)_6$ precursor with high magnification image in the inset. (b) SEM and (c) TEM images of CSVC-NC. (d) SEM image, (e) corresponding high magnification image, (f) TEM, (g) HRTEM, (h) SEAD pattern, (i) HAADF-STEM images and the corresponding elemental mapping of CSVC-NB.

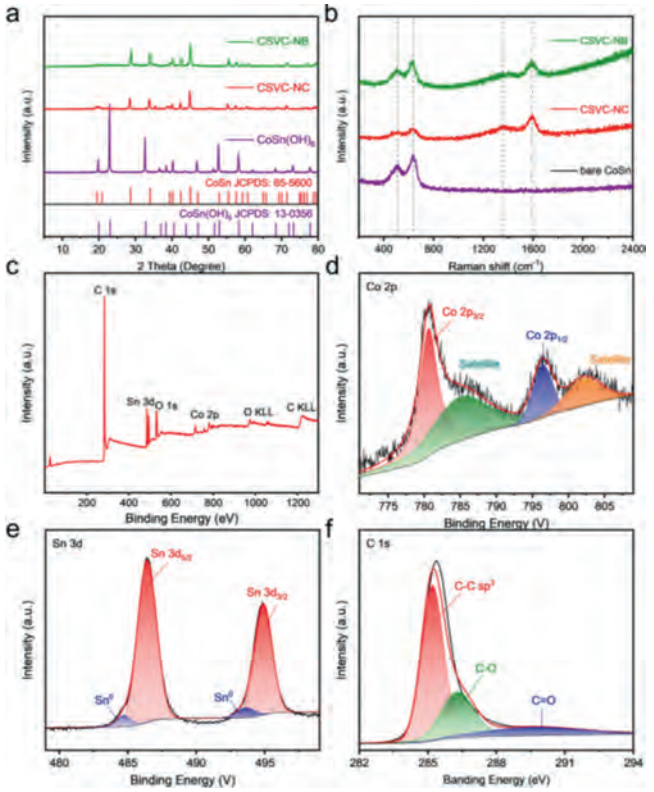

Fig. 2. (a) XRD patterns of $CoSn(OH)_6$ precursor, CSVC-NC and CSVC-NB. (b) Raman spectrum of CSVC-NB, CSVC-NC and bare CoSn. (c) XPS survey spectra of CSVC-NB. XPS spectrum of (d) Co 2p, (e) Sn 3d and (f) C 1 s.

picted in Figs. 1b–f. As can be seen, the three-dimensional structure inherited from the $CoSn(OH)_6$ precursor is well maintained after hydrothermal and heat treatment. An 8–10 nm carbon shell is clearly observed and Co and Sn atoms are entirely encapsulated in the framework. It is the amphoteric nature of $CoSn(OH)_6$ that determines the formation of soluble $[Co(OH)_4]^{2-}$ and $[Sn(OH)_6]^{2-}$ due to the existence of excess OH^- (Eq. 2). Thermodynamically, $[Co(OH)_4]^{2-}$ is easily oxidized in air, which can lead to the formation of an insoluble outer boundary layer of solid CoOOH, and as a result, it prevent continuous oxidation of $[Co(OH)_4]^{2-}$ species during the alkaline etching (Eq. 3). Thus, the hollow structure of nanoboxes can be distinctly observed from the cracked $CoSn(OH)_6$ cubes without any obvious impurities in the insert of Figs. 1d and e. The passivation layer, identified as CoOOH, on the outer surface of the cubes and hollow interior geometrical structure are carried out directly by TEM, as shown in Fig. 1f. The porous layer and sufficient void spaces not only provide abundant reactive sites but also render space to withstand the volume variation of the CoSn cores. The high-resolution TEM (HR-TEM) image (Fig. 1g) indicates that the CoSn bimetallic grains exhibit irregular shape with a diameter of 15–20 nm and are completely encapsulated into the amorphous carbon layer. The interplanar distance of lattice fringes is measured to be 0.31 nm, corresponding to the (101) crystal plane of CoSn. Another two crystal planes of (110) and (201) are also be confirmed by the SEAD pattern in Fig. 1h. High-angle annular dark field (HAADF) and STEM-EDS mapping images in Fig. 1i display a uniform distribution of Co, Sn and C elements, suggesting that the metallic Co and Sn are homogeneously distributed in the carbon shell with a distinct hollow structure.

$$Co^{2+} + Sn^{4+} + 6OH^- \longrightarrow CoSn(OH)_6\ (s) \quad (1)$$

$$CoSn(OH)_6 + 4OH^- \longrightarrow [Co(OH)_4]^{2-} + [Sn(OH)_6]^{2-} \quad (2)$$

$$4[Co(OH)_4]^{2-} + O_2 \longrightarrow 4CoOOH\ (s) + 2H_2O + 8OH^- \quad (3)$$

In order to analyze the crystal structure and phase purity, Fig. 2a provides the XRD peaks of $CoSn(OH)_6$ precursor, the as-synthesized CSVC-NC and CSVC-NB. All the peaks of the precursor can be well-matched with the standard patterns of perovskite-type $CoSn(OH)_6$ (JCPDS No. 13-0356), demonstrating a high degree of crystallization and purity [41]. The CoOOH phase can hardly be examined because of the small mass fraction of this layer in a short reaction time. As can be seen, the XRD peaks of samples after annealing are totally different from those of the precursor, which is highly converted to the peaks of alloy CoSn (JCPDS No. 65-5600). There are no peaks of any impurities, confirming the sufficient synthesis of intermetallic CoSn compounds. However, the diffraction peaks of carbon and SiO_2 in Fig. S2 (Supporting information) can be hardly observed because of their weak crystalline nature. The graphitization of carbon can be detected by the Raman spectrum of CSVC-NC and CSVC-NB, as shown in Fig. 2b. It is notable that two characteristic peaks of graphitic carbon corresponding to D and G bands are situated at about 1369 cm^{-1} and 1585 cm^{-1}, where D band and G band represent the disorders and defects of crystals and the vibration of sp^2 carbon atoms, respectively [42]. Moreover, the previous reports indicated that transition elements, such as Co, could perform the significant catalytic effect to transform the amorphous carbon into graphitic carbon, hence the value of I_D/I_G for CSVC-NC and CSVC-NB is relatively small, only about 0.6 [43,44]. Besides, the peaks located at 504 cm^{-1} and 633 cm^{-1} can be ascribed to the existence of bimetallic CoSn, further supporting the multicore and carbon shell structure of the samples [45]. The thermogravimetric analysis (TGA) was used to estimate the contents of alloys and carbon in the CSVC-NC and CSVC-NB, as shown in Fig. S3 (Supporting information). The initial weight loss below 200 °C is ascribed to the removal of physisorbed and chemisorbed water. The mass loss between 300 °C and 450 °C

should be assigned to consumption of carbon under the air atmosphere. Interestingly, a weight rise could be both observed below 300 °C and above 500 °C, respectively, which may be caused by the partial oxidation of CoSn to CoO_x and SnO_x and the prolonged oxidation of CoO_x and SnO_x to SnO_2/Co_3O_4. After calculating, the carbon contents of CSVC-NB and CSVC-NC are calculated to be 41.44% and 20.14%. Moreover, the nitrogen absorption-desorption measurements were utilized for the sake of detecting the surface area and specific pore features of the two samples. As exhibited in Fig. S4 (Supporting information), the isotherm with a hysteresis at high relative pressures is typical type-IV behavior with BET surface areas of 57.1 m^2/g and 14.0 m^2/g of CSVC-NB and CSVC-NC, respectively. Besides, the samples all show pore size of ~2–10 nm, elucidating a typical mesoporous structure.

The X-ray photoelectron spectroscopy (XPS) survey spectra (Fig. 2c) are also recorded to identify the elementary composition and the valence state of the surface layer for CSVC-NB. It is worth noting that the partial oxidation of Co^{2+} and Sn^{4+} leads to the presence of the O peaks, while the rare Co and Sn oxide can hardly be detected in the XRD patterns. The typical high-resolution spectra of Co 2p, Sn 3d and C 1s are probed in Figs. 2d–f, respectively. Two typical peaks located at 780.6 eV and 796.4 eV in the Co 2p spectrum (Fig. 2d) are split to Co $2p_{3/2}$ and Co $2p_{1/2}$ states with two corresponding satellites caused by spin-orbit, indicating the existence of Co^{2+} [46,47]. The Sn 3d spectrum in Fig. 2e obviously exhibit two major peaks at 486.4 eV (Sn $3d_{5/2}$) and 495.0 eV (Sn $3d_{3/2}$), which can be assigned to a Sn^{4+} oxidized state due to the exposure to air. Meanwhile, two peaks at 484.7 eV and 493.6 eV are indexed into Sn^0 of CoSn nanoparticles [48,49]. The high-resolution C 1s region in Fig. 2f displays an arresting peak at 284.8 eV, which was mainly derived from the C sp^3 hybrid orbitals. The C–O and C=O bonds are represented by another two peaks exactly centered at 286.3 eV and 289.6 eV [50]. The XPS also offers the surface atoms ratio (Co:Sn = 1:1) of the samples, corresponding with the result of EDS spectrum in Fig. S5 (Supporting information), which indicates that there is no loss of atoms during the entire preparation process. It is also certificated that SiO_2 layer was completely etched by NaOH in the final product.

The electrochemical performances of CSVC-NC and CSVC-NB were evaluated in Li-ion half-cell configurations with lithium metal as both counter and reference electrodes. The cyclic voltammetry (CV) curves of CSVC-NB for the initial 5 cycles are displayed in Fig. 3a, with a potential window of 0.01–3.0 V *versus* Li^+/Li. According to the first cathodic scan, there are two peaks at 0.6 V ascribed to the conformation of the solid electrolyte interphase (SEI) film and the formation of the Li_ySn alloy from the reaction of the CoSn nanoparticles with Li ion (Eq. 4) [50]. It is notable that the peak disappears in the next following cycles, which can be assigned to the irreversibility of SEI. Afterwards, the peak corresponding to the alloying with Li^+ shifts to 0.89 V. During the anodic scans, an obvious peak situated at ~0.55 V demonstrates the dealloying of Li_ySn (Eq. 5). The peaks at 1.35 V and 2.05 V are approximately attributed to the partial surface oxidation of CoSn alloy and the carbon shell [22]. From the second cycle onwards, the overlapping CV curves confirm the superior reversibility and stability of the electrode. Practically, the possible chemical reactions of the CV profiles are described as follows:

$$Co_xSn + yLi^+ + ye^- \longrightarrow xCo + Li_ySn\ (0 \le x \le 1,\ 0 \le y \le 4.4) \quad (4)$$

$$Sn + yLi^+ + ye^- \longleftrightarrow Li_ySn \quad (5)$$

Fig. 3b shows the galvanostatic charge and discharge (GCD) profiles of CSVC-NB at the current density of 100 mA/g. Specifically, the inflection points of discharge/charge plateaus are strongly in accordance with the CV curves, as marked with the dotted box.

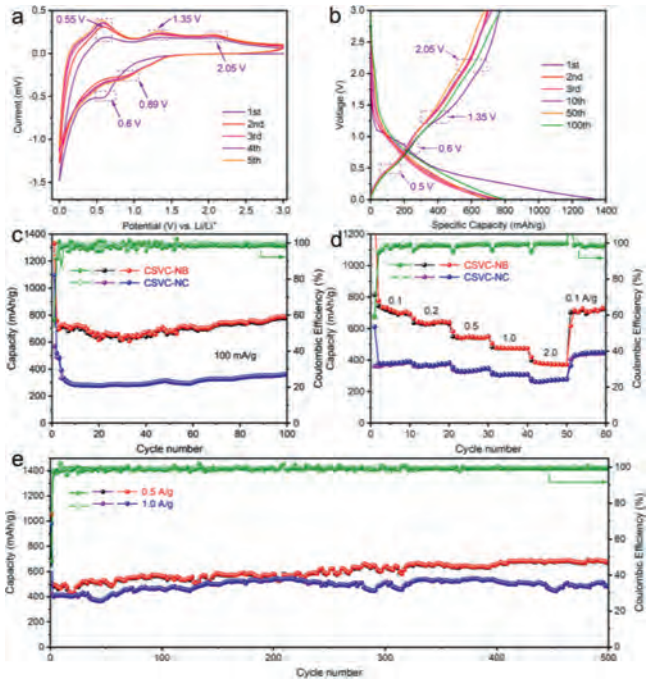

Fig. 3. Electrochemical performance of CSVC-NB. (a) Cyclic voltammetry curves. (b) Galvanostatic discharge-charge profiles at 100 mA/g. (c) Cycling performance at 100 mA/g. (d) Rate performance profiles from 0.1 A/g to 2.0 A/g. (e) Long-term cycling performance for CSVC-NB at 0.5 A/g and 1.0 A/g.

The low discharge plateau or platform of anode materials confirms the practical value of this material [14,22]. The initial discharge and charge capacities of CSVS-NB exhibit as 1331.4 mAh/g and 766.7 mAh/g with an initial Coulombic efficiency (ICE) of 57.6%. In comparison with the CSVC-NC and bare CoSn anode materials, the ICEs are nearly 51.2% and 42.4% corresponding to the initial discharge capacities of 1096.8 mAh/g and 147.6 mAh/g, respectively. Actually, the loss of irreversible capacities is associated with the formation of SEI layers and an irreversible oxidation reaction on the surface. After the second cycle, the CE rapidly approaches to relatively 100%, revealing the excellent reversibility and marvelous cyclic stability of the CSVC-NB during delithiation/lithiation process. Moreover, the cycle performances of the CSVC-NB, CSVC-NC and bare CoSn at the current density of 100 mA/g are displayed in Fig. 3c and Fig. S6 (Supporting information). The CSVC-NB composite delivers a reversible capacity of 788.2 mAh/g even after 100 cycles superior to the CSVC-NC (366.1 mAh/g) and bare CoSn (173.1 mAh/g), which can be attributed to the well-designed multi-core structure and the constraint action of the carbon shell. The result ulteriorly confirms that the nanobox structure and the multi-cores provide the extra space to alleviate the volume expansion and additional mechanical stress during the repeated electrochemical reactions. Without the protection of the carbon shell and the interconnected transmission channels, the bare CoSn electrode is much easier to agglomerate together and pulverize, ultimately leading to the severe decrease of inconvertible capacities.

The rate performances of the CSVC-NB and CSVC-NC were conducted at multiple current rates ranging from 0.1 A/g to 2 A/g, proving that the CSVC-NB exceeds the CSVC-NC electrode. As shown in Fig. 3d, the discharge capacities of the CSVC-NB composite are 693.0, 639.9, 547.4, 474.5, 372.0 mAh/g and then recovers to 729.5 mAh/g when the current density rebounds to 0.1 A/g, which exhibits the remarkable reversible capacity and cycling stability. The electrochemical performances are still associ-

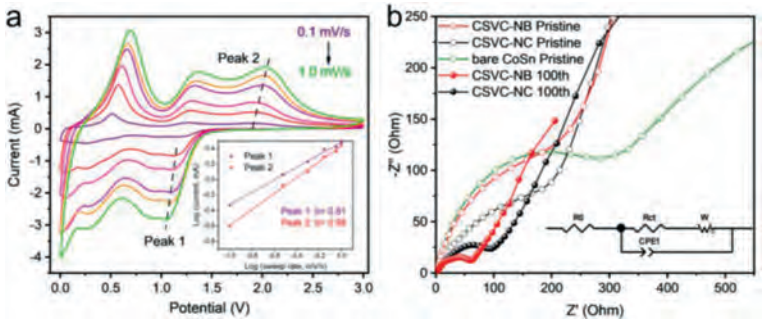

Fig. 4. (a) Cyclic voltammetry curves of CSVC-NB at different scan rates from 0.1 mV/s to 1.0 mV/s, with the fitted linear relationship between log*v* and log*i* in the inset. (b) Nyquist plots of the electrodes before and after 100 cycles at 100 mA/g.

ated with the size of nanoparticles, the abundant voids and the porous carbon shell, which enhance the diffusion of Li ions and charge transfer. To further testify the inspiring reversible performance of the regulated structure, the long-life cycling performance was also tested at the current density of 0.5 A/g and 1 A/g, delivering the stable capacity of 645.0 mAh/g and 519.2 mAh/g after 300 cycles, respectively. The CE of the second cycle rise to 94.3%, 87.1% and subsequently maintains over 98%. Interestingly, a common phenomenon is found that the capacity decreases for the first several cycles and then increases slightly, which has been reported previously in Sn-based anodes and other metal oxide anodes. It is considered to the formation of a gel-like thin film, pseudocapacitive contribution, continuous restructuration and activation reactions during the discharge/charge process [22,51]. Furthermore, the morphology and inner structure after 100 cycles were investigated by SEM and TEM, as shown in Figs. S7 and S8 (Supporting information). The cubic structure of CSVC-NB is well maintained (Fig. S7d), which is attributed to the reduction of mechanical stress and relaxation of volume expansion owing to the decreased particle size. Besides, the well-maintained structure without pulverization forcefully demonstrates the preeminent structural stability of the 3D multicore-shell composites.

Besides, the capacity contribution and charge kinetic process of CSVC-NB electrode were further investigated by CV curves at different scan rates ranging from 0.1 mV/s to 1.0 mV/s, as shown in Fig. 4a. Obviously, the CV curves display similar shapes with slightly shifting and widening. Empirically, the measured current (i) has a functional relationship with the scan rates (v) expressed as follows:

$$i = av^b \tag{6}$$

where both a and b are constant. The previous reports expounded that b is equivalent to the slope of the logarithm of peak current (log$i$) versus the logarithm of sweep rate (log$v$), and can also characterized the charge storage mechanism [52–54]. When b value is close to 0.5, it exhibits an ideal diffusion-controlled process, meanwhile the capacitive-controlled process is implied when b is nearer to 1 [55]. From the linear fitted result in the inset of Fig. 4a, the b values at peak 1 and 2 are calculated to be 0.81 and 0.98, respectively, which demonstrates that the pseudocapacitive process with a fast kinetics contributes dominantly during the electrochemical reactions of electrodes. The contribution rates of pseudocapacitance of CSVC-NB and CSVC-NC are calculated to deeply investigate the intrinsic charge storage kinetics. After calculating, 63.2% of the total capacity is regarded as the ratio of capacitive contribution at 0.5 mV/s (Fig. S9 in Supporting information), which is smaller than 70.1% of CSVC-NB, proving that the hollow structure and CoSn nanoparticles are more favorable for electron transport and particle diffusion.

Moreover, the charge transfer behavior and the ionic diffusion resistance of the electrode at the electrode-electrolyte interface were carried out by electrochemical impedance spectroscopy (EIS) in the frequency range from 100 kHz to 10 mHz. Usually, the Nyquist plot consists of a semicircle at the high-frequency region representing the charge transfer resistance for Li-ion insertion to the active materials, and an inclined line at the low-frequency region for Li-ion diffusion in the electrolyte. Besides, the corresponding equivalent electric circuit is depicted in the inset, where R_0 represents the resistance of electrolyte and W is the Warburg resistance [56]. Totally different from the almost identical curves of pristine electrodes, the diameter of the semicircle of CSVC-NB after 100 cycles is much smaller than that of CSVC-NC, reflecting a lower charge transfer impedance (R_{ct}), as shown in the high-frequency region of the Nyquist plots in Fig. 4b and Table S1 (Supporting information). The significant reduction of the diameter of semicircle is attributed to the stable formation of SEI layer and the effective migration of the lithium ions and electrons in favor of the outstanding electrochemical properties of CSVC-NB.

In summary, a 3D multicore-shell nanobox structure of CoSn@void@C was successfully fabricated by a facile hydrothermal method with SiO_2 as a sacrificial agent. The chemical buffer effect of inactive Co, the extra void space and the elaborated carbon layer not only provide high tolerance to volume change during the lithiation procedure improving the structural stability, but also prevent the agglomeration of CoSn nanoparticles and ensure the remarkable electronic and ionic conductivities. As a result, the anticipated anode of CSVC-NB manifests the robust electrochemical superiorities, including the high specific capacity of 788.2 mAh/g after 100 cycles and long-term cycling stability of 519.2 mAh/g at 1 A/g after 300 cycles. The synthetic route and great properties of this material show a broad prospect in next-generation lithium-ion batteries, and can be extended to fabricate other alloyed electrode materials (Ni, Sb, Fe, Cu, *etc.*) with multicore-shell nanobox structure.

Declaration of competing interest

The authors declare that they have no known competing financial interests or personal relationships that could have appeared to influence the work reported in this paper.

Acknowledgments

The authors acknowledge the financial support by National Natural Science Foundation of China (Nos. U20A20123, 51874357, 52002405), Innovative Research Group of Hunan Provincial Natural Science Foundation of China (No. 2019JJ10006). G. Chen acknowledges the support from the 100 Talented Program of

Hunan Province and “Huxiang High-level Talents” Program (No. 2019RS1007).

Supplementary materials

Supplementary material associated with this article can be found, in the online version, at doi:10.1016/j.cclet.2021.11.021.

References

[1] R.C. Massé, E. Uchaker, G. Cao, Sci. China Mater. 58 (2015) 715–766.
[2] E. Uchaker, G. Cao, Nano Today 9 (2014) 499–524.
[3] A. Fotouhi, D.J. Auger, K. Propp, et al., Renew. Sustain. Energy Rev. 56 (2016) 1008–1021.
[4] G. Chen, L. Yan, H. Luo, S. Guo, Adv. Mater. 28 (2016) 7580–7602.
[5] G. Harper, R. Sommerville, E. Kendrick, et al., Nature 575 (2019) 75–86.
[6] T.H. Kim, J.S. Park, S.K. Chang, et al., Adv. Energy Mater. 2 (2012) 860–872.
[7] Y. Ma, U. Ulissi, D. Bresser, et al., Electrochim. Acta 258 (2017) 535–543.
[8] K. Kravchyk, L. Protesescu, M.I. Bodnarchuk, et al., J. Am. Chem. Soc. 135 (2013) 4199–4202.
[9] X. Zhou, L. Yu, X.Y. Yu, X.W. Lou, Adv. Energy Mater. 6 (2016) 1601177.
[10] X. Zhou, J. Bao, Z. Dai, Y.G. Guo, J. Phys. Chem. C 117 (2013) 25367–25373.
[11] X. Kong, J. Zhang, J. Huang, et al., Chin. Chem. Lett. 30 (2019) 771–774.
[12] P. Sun, J. Davis, L. Cao, et al., Energy Storage Mater. 17 (2019) 151–156.
[13] Y. Guo, X. Zeng, Y. Zhang, et al., ACS Appl. Mater. Interfaces 9 (2017) 17172–17177.
[14] J. Pu, H. Du, J. Wang, et al., J. Power Sources 360 (2017) 189–195.
[15] W.H. Li, X.L. Sun, Y. Yu, Small Methods 1 (2017) 1600037.
[16] H.H. Cho, M.P.B. Glazer, D.C. Dunand, ACS Appl. Mater. Interfaces 9 (2017) 15433–15438.
[17] X. Li, X. He, Y. Xu, et al., J. Mater. Chem. A 3 (2015) 3794–3800.
[18] M.G. Park, D.H. Lee, H. Jung, et al., ACS Nano 12 (2018) 2955–2967.
[19] W. Tang, J. Jian, G. Chen, et al., Energy Mater. Adv. 2021 (2021) 8140964.
[20] T.L. Nguyen, D.S. Kim, J. Hur, et al., Electrochim. Acta 278 (2018) 25–32.
[21] H. Ying, W.Q. Han, Adv. Sci. 4 (2017) 1700298.
[22] H. Zhang, X. Huang, O. Noonan, et al., Adv. Funct. Mater. 27 (2017) 1606023.
[23] S. Kang, X. Chen, J. Niu, Nano Lett. 18 (2018) 467–474.
[24] L. Ma, P. Yan, S. Wu, et al., J. Mater. Chem. A 5 (2017) 16994–17000.
[25] Y. Fu, X. Gao, D. Zha, et al., J. Mater. Chem. A 6 (2018) 1601–1611.
[26] H. Tian, F. Xin, X. Wang, et al., J. Mater. 1 (2015) 153–169.
[27] J. Liu, L. Yu, C. Wu, et al., Nano Lett. 17 (2017) 2034–2042.
[28] C. Chen, X. Zheng, J. Yang, M. Wei, Phys. Chem. Chem. Phys. 16 (2014) 20073–20078.
[29] J. Kramer, B. Kelly, V. Manivannan, Open Chem. 8 (2010) 65–69.
[30] X.L. Wang, W.Q. Han, J. Chen, J. Graetz, ACS Appl. Mater. Interfaces 2 (2010) 1548–1551.
[31] J. Li, X. Xu, Z. Luo, et al., Electrochim. Acta 304 (2019) 246–254.
[32] P. Nithyadharseni, M.V. Reddy, B. Nalini, et al., Electrochim. Acta 161 (2015) 261–268.
[33] G.O. Park, J. Yoon, J.K. Shon, et al., Adv. Funct. Mater. 26 (2016) 2800–2808.
[34] Y. Tong, H. Liu, M. Dai, et al., Chin. Chem. Lett. 31 (2020) 2295–2299.
[35] W. Lu, X. Guo, Y. Luo, et al., Chem. Eng. J. 355 (2019) 208–237.
[36] Y. Fang, X.Y. Yu, X.W.D. Lou, Adv. Mater. 30 (2018) e1706668.
[37] J. Wang, W. Li, F. Wang, et al., Nanoscale 6 (2014) 3217–3222.
[38] B. Huang, X. Li, Y. Pei, et al., Small 12 (2016) 1945–1955.
[39] Z. Wang, Z. Wang, H. Wu, X.W. Lou, Sci. Rep. 3 (2013) 1391.
[40] W. Stöber, A. Fink, E. Bohn, J. Colloid Interface Sci. 26 (1968) 62–69.
[41] F. Song, K. Schenk, X. Hu, Energy Environ. Sci. 9 (2016) 473–477.
[42] A.C. Ferrari, D.M. Basko, Nat. Nanotechnol. 8 (2013) 235–246.
[43] A. Ōya, S. Ōtani, Carbon 17 (1979) 131–137.
[44] J. Shin, W.H. Ryu, K.S. Park, I.D. Kim, ACS Nano 7 (2013) 7330–7341.
[45] I.I. Gontia, M. Baibarac, I. Baltog, Phys. Status Solidi B 248 (2011) 1494–1498.
[46] Y. Bian, R. Wang, S. Wang, et al., J. Mater. Chem. A 6 (2018) 15807–15814.
[47] Y. Bian, S. Wang, D. Jin, et al., Nano Energy 75 (2020) 104935.
[48] H. Zhu, D.C. Rosenfeld, M. Harb, et al., ACS Catal. 6 (2016) 2852–2866.
[49] W. Wang, D. Lei, Y. Dong, et al., Sci. Rep. 7 (2017) 1835.
[50] C.M. Park, J.H. Kim, H. Kim, H.J. Sohn, Chem. Soc. Rev. 39 (2010) 3115–3141.
[51] J. Qin, D. Liu, X. Zhang, et al., Nanoscale 9 (2017) 15856–15864.
[52] X. Xu, J. Liu, J. Liu, et al., Adv. Funct. Mater. 28 (2018) 1707573.
[53] T. Brezesinski, J. Wang, S.H. Tolbert, B. Dunn, Nat. Mater. 9 (2010) 146–151.
[54] H.-S. Kim, J.B. Cook, S.H. Tolbert, B. Dunn, J. Electrochem. Soc. 162 (2015) A5083–A5090.
[55] J. Li, X. Xu, X. Yu, et al., ACS Appl. Mater. Interfaces 12 (2020) 4414–4422.
[56] A.R. Park, C.M. Park, ACS Nano 11 (2017) 6074–6084.